

# Temporal multilayer structures in discrete physical systems towards arbitrary-dimensional non-Abelian Aharonov-Bohm interferences

Received: 25 November 2023

Accepted: 14 August 2024

Published online: 27 August 2024

 Check for updates

Zhaohui Dong <sup>1</sup>, Xiaoxiong Wu<sup>1</sup>, Yiwen Yang<sup>1</sup>, Penghong Yu<sup>1</sup>,  
Xianfeng Chen <sup>1,2,3</sup> & Luqi Yuan <sup>1</sup> 

Temporal modulation recently draws great attentions in wave manipulations, with which one can introduce the concept of temporal multilayer structure, a temporal counterpart of spatially multilayer configurations. This kind of multilayer structure holds temporal interfaces in the time domain, which provides additional flexibility in temporal operations. Here we take this opportunity and propose to simulate a non-Abelian gauge field with a temporal multilayer structure in the discrete physical system. Two basic temporal operations, i.e., the folding/unfolding operation and the phase shift operation are used to design such a temporal multilayer structure, which hence can support noncommutative operations to realize the non-Abelian Aharonov-Bohm interference in the time domain. A two-/three-dimensional non-Abelian gauge field can be built, which may be further extended to higher dimensions. Our work therefore provides a unique platform enabling generalization of non-Abelian physics to arbitrary dimensions and offers a method for wave manipulations with temporal band engineering.

Temporal modulations have recently emerged as a powerful tool for wave manipulations<sup>1–4</sup> and hence stimulate growing interest in the electromagnetic community. As a typical operation in temporal modulations, when a system experiences a change of material properties abruptly in time and uniformly in space with its timescale comparable to the period of the electromagnetic wave, the so-called temporal interface (TI)<sup>5,6</sup> is created. Unlike its spatial counterpart (i.e. spatial boundary), the system holds the translational symmetry at TI while the time-reversal symmetry is broken, thus providing intriguing opportunities for exploring novel scattering features in controlling waves<sup>7–10</sup>. If multiple TIs are aligned sequentially, a temporal multilayer structure can be built<sup>11</sup>, and a variety of promising applications are unveiled including temporal aiming<sup>12</sup>, antireflection temporal

coating<sup>13</sup>, frequency conversion<sup>14</sup>, and temporal optical activity<sup>15</sup>. In analogy to continuous electromagnetic systems, one can introduce TI by abruptly varying the configuration of the lattice<sup>16–20</sup> in discrete systems where the field can be expanded by a set of finite, discrete set of bound states or modes<sup>21</sup>. Fruitful implementations are also conceivable by using multiple TIs in these discrete systems, such as tunable temporal cloaking<sup>17</sup>, temporal beam encoder<sup>19</sup> and temporal interference<sup>20</sup>. Therefore, cascade TIs offer a unique opportunity to explore new electromagnetic phenomena in discrete systems.

On the other hand, the Aharonov-Bohm (AB) interference shows a crucial verification of the physical consequences of gauge fields<sup>22,23</sup>, and hence is a long-standing important research subject in physics<sup>24</sup>. In particular, recently, there has been emerging interest in synthesizing

<sup>1</sup>State Key Laboratory of Advanced Optical Communication Systems and Networks, School of Physics and Astronomy, Shanghai Jiao Tong University, Shanghai, China. <sup>2</sup>Shanghai Research Center for Quantum Sciences, Shanghai, China. <sup>3</sup>Collaborative Innovation Center of Light Manipulation and Applications, Shandong Normal University, Jinan, China. ✉e-mail: [yuanluqi@sjtu.edu.cn](mailto:yuanluqi@sjtu.edu.cn)

non-Abelian gauge fields to explore novel phenomena<sup>25–29</sup>, and the resulting non-Abelian AB interference<sup>30–33</sup>, therefore, becomes an important example of non-Abelian effects that is important to topological quantum computing<sup>34</sup>. It is of fundamental interest to find a flexible way to construct non-Abelian AB interference and push such effect into higher-dimensional gauge-field cases. Obviously, the operation of TIs in electromagnetic systems holds the potential in accomplishing such a task, which demands the study.

In this paper, we tackle this problem by utilizing the concept of temporal multilayer structure by introducing cascade TIs in the discrete tight-binding model. We explore a temporal interference of degenerate states, and further develop it into an AB interference under a temporal non-Abelian gauge field using the construction with two types of TIs. Such a non-Abelian gauge field can be achieved by leveraging the temporal degenerate-state interference created by TI operations. Both SU(2) and SU(3) non-Abelian gauge fields are studied in theory and are verified by simulations, which can potentially be extended to a SU( $N$ ) one. Our work reveals that noncommutative operations can be performed in a temporal multilayer structure which further empowers wave manipulation by temporal engineering systems. Besides, the proposed method of non-Abelian AB interference holds unique features compared to previous works<sup>25,27,32,33</sup> (see supplementary material Section I), which enables the extension to a higher dimensional gauge field, and, therefore, offers a way of studying high-dimensional non-Abelian gauge field-related physics in the time domain.

## Results

### Temporal multilayer structure and two types of TIs

We first introduce the concept of the temporal multilayer structure and its usage in wave manipulations. A simple example is illustrated in

Fig. 1a, where the system experiences two TIs during the evolution of wave pulse. Suppose the pulse having an initial eigenstate of the system ( $\omega_n, k$ ) is injected at  $t=0$ , where  $\omega_n$  represents the quasi-energy,  $n$  denotes the band index, and  $k$  represents the quasi-momentum. When the first TI occurs, the structure of the system changes, and the eigenstate varies into the new ones  $\{(\omega'_n, k)\}$ . Therefore, the input pulse projected into the new eigenstates while the momentum  $k$  still conserves as the system holds translational symmetry. One can expect that if there are multiple bands ( $n > 1$ ), different projections of the pulse onto different bands experience evolutions with different group velocities, so the pulse can be divided into multiple parts which accumulate different phases during evolutions due to the difference in their quasi-energies. We now assume the second TI occurs, and the system changes back to the original one. Under this operation, instead of getting projected onto the original eigenstate ( $\omega_n, k$ ), the pulse with eigenstates  $\{(\omega'_n, k)\}$  is actually projected onto all the eigenstates  $\{(\omega_n, k)\}$ . Therefore, by judicious engineering the temporal multilayer structure, one can obtain the desired final state of the wave. Such temporal architecture exploits various degrees of freedom of the system offered by multiple and even different types of TIs, which enables advanced wave controls. Moreover, the system under multiple temporal operations can be discrete in model, which offers a versatile platform for a diverse family of TIs thanks to the flexibility in controlling lattice structures through on-site gain or loss<sup>35</sup>, coupling phases<sup>16</sup>, and strengths<sup>18</sup>, and more importantly provides possible experimental feasibility compared to its continuous counterparts<sup>17,19,20</sup>.

Next, we introduce two simple temporal operations as two types of TIs, which are building blocks of the temporal multilayer structure in our study. The first one is the band-folding/band-unfolding operation (see Fig. 1b). Consider two lattice models which are described by

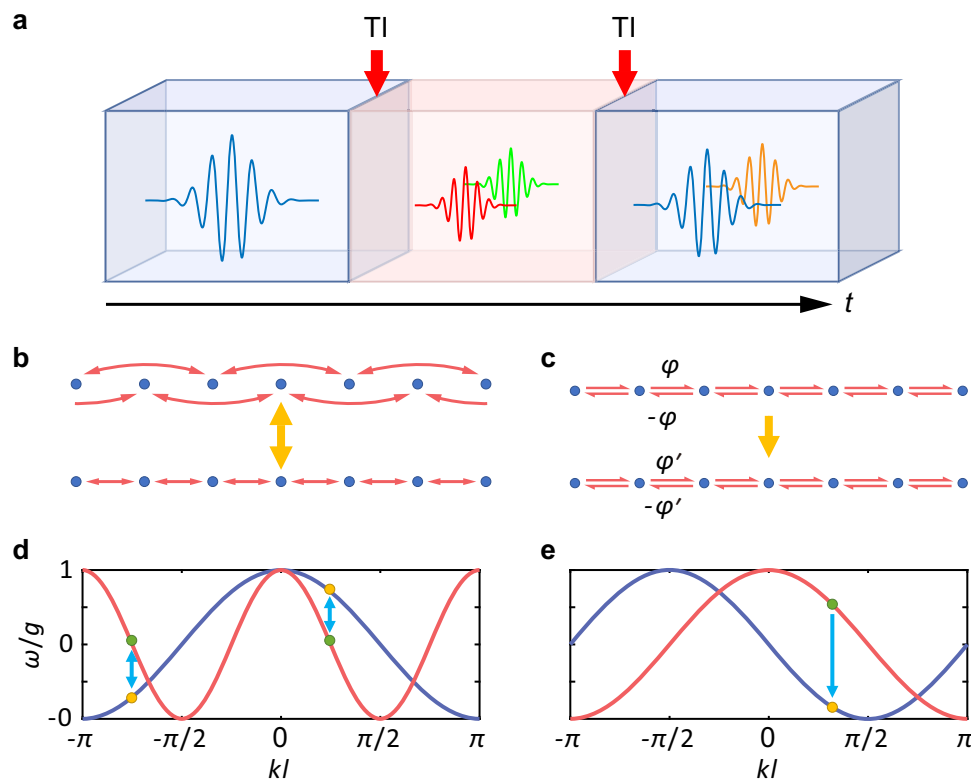


**Fig. 1 | Wave evolution in a temporal multilayer structure and two kinds of TIs.** **a** Illustration of the concept of a temporal multilayer structure, where a wave evolves inside a discrete system experiencing two TIs at different times. Schematic operations of band-unfolding (and band-folding as the inverse operation) and band

shifting. **b, c** Changes of the lattice structure by changing the ranges of couplings or coupling phase for realizing operations. **d, e** Changes of the states and band structures accordingly. Red (violet) lines are the bandstructures before (after) the TI. Green (yellow) dots denote the states before (after) the TI.

Hamiltonians

$$H_1 = g \sum_m (e^{-i\varphi} a_m^\dagger a_{m+1} + e^{i\varphi} a_{m+1}^\dagger a_m), \tag{1}$$

$$H_2 = g \sum_m (e^{-i\varphi} a_m^\dagger a_{m+2} + e^{i\varphi} a_{m+2}^\dagger a_m). \tag{2}$$

where  $g$  is the coupling strength,  $a_m$  ( $a_m^\dagger$ ) is the annihilation (creation) operator at the  $m$ -th lattice site, and  $\varphi$  is the coupling phase. The lattice constants of  $H_1$  and  $H_2$  are  $l$  and  $2l$ , respectively, i.e.,  $H_1$  includes only the nearest-neighbor hoppings while  $H_2$  includes only the next-nearest-neighbor hoppings. In particular, the Hamiltonian  $H_2$  can be split into two individual sublattices which only contain the even number sites or odd number sites with lattice constant  $2l$ ,

$$H_2 = g \sum_{m \in 2n} (e^{-i\varphi} a_m^\dagger a_{m+2} + e^{i\varphi} a_{m+2}^\dagger a_m) + g \sum_{m \in 2n+1} (e^{-i\varphi} a_m^\dagger a_{m+2} + e^{i\varphi} a_{m+2}^\dagger a_m), \tag{3}$$

where  $n$  is an integer, and therefore the system supports a twofold degenerate state for given  $\omega$  and  $k$ , whose eigenstates can be written in the odd number site basis with  $(1, 0)^T$  (i.e., odd-distributed mode) and even number site basis with  $(0, 1)^T$  (i.e., even-distributed mode), respectively. The two Hamiltonians  $H_2$  and  $H_1$  can be interconverted by the operation of band-folding/band-unfolding by changing the range of all couplings between sites from  $\{l\}$  to  $\{l_r/s\}$ . Here, both  $\{l_r\}$  and  $\{l_r/s\}$  denote the coupling range. Particularly,  $l_r$  ( $l_r/s$ ) represents the range of couplings between sites and their  $l_r$ -th ( $l_r/s$ -th) nearest neighbors, which is a positive integer.  $s$  is the scaling factor of band folding or unfolding. We take the band-unfolding operation shown in Fig. 1b as an example. Such operation transforms  $H_2$  to  $H_1$  by varying the next-nearest neighboring couplings to the nearest neighboring ones for all sites, corresponding to  $\{l_r\} = \{2\}$  and  $s=2$ . After the band-unfolding operation, the first Brillouin zone is expanded from  $[-\pi/2l, \pi/2l]$  to  $[-\pi/l, \pi/l]$ , and an initial eigenstate  $(\omega, k)$  (with  $k=k_0 + r\pi/l$ , where  $k_0 \in [-\pi/2l, \pi/2l]$  and  $r$  is an integer) marked by the green dots on the red band projects onto two different eigenstates  $(\omega_{1,2}, k_{1,2})$  (with  $k_1=k_0 + 2r\pi/l$  and  $k_2=k_1 + \pi/l$ ) shown as the yellow dots on the violet band with different group velocities in Fig. 1d. Such a phenomenon is the result from the change of the lattice constant in discrete systems. Due to the translational symmetry of the lattice in Eq. (3), the two initial eigenstates  $(\omega, k_1)$  and  $(\omega, k_2)$  are indistinguishable. However, when the lattice constant changes from  $2l$  to  $l$  in the model, i.e.,  $H_2$  is changed to  $H_1$ , the two projected eigenstates are distinguishable as the first Brillouin zone is expanded. Therefore, after this type of TI, we can represent the wave state in a new basis, where  $(1, 0)^T$  represents the  $k_1$  mode and  $(0, 1)^T$  represents the  $k_2$  mode. If we assume the wave state before the TI as  $(I_o, I_e)^T$  in the odd/even-distributed mode basis and the wave state after the TI as  $(O_{k_1}, O_{k_2})^T$  in the  $k_1/k_2$  mode basis, the input-output relation of this band-unfolding operation can be written by

$$\begin{pmatrix} O_{k_1} \\ O_{k_2} \end{pmatrix} = \frac{1}{\sqrt{2}} \begin{pmatrix} 1 & 1 \\ 1 & -1 \end{pmatrix} \begin{pmatrix} I_o \\ I_e \end{pmatrix}, \tag{4}$$

whose derivation is given in Methods. Similarly, the band-folding operation as the inverse operation of the band-unfolding one, changes the short-range couplings to the long-range ones, i.e.,  $H_1$  is changed to  $H_2$ , which folds the first Brillouin zone, and hence the eigenstates  $(\omega_{1,2}, k_{1,2})$  project onto the twofold degenerate state, where the mathematical description is the inverse function of Eq. (4).

The second temporal operation is the band shifting, illustrated in Fig. 1c, corresponding to the operation that the TI occurs at  $t = t_0$  with the coupling phase changed from  $\varphi$  to  $\varphi' = \varphi + \Delta\varphi$  on the Hamiltonian

$H_1$ . The bandstructure then becomes

$$\omega = 2g \cos(k - \varphi') = 2g \cos(k - \varphi - \Delta\varphi), \tag{5}$$

which is shifted by  $\Delta\varphi$  in the  $k$ -axis. Such band shifting is related to the change of the effective vector potential  $\mathbf{A}$  introduced by  $\varphi$ , which is linked to  $\varphi$  with the expression<sup>36</sup>

$$\varphi = \int_m^{m+1} \mathbf{A} \cdot d\mathbf{l}, \tag{6}$$

where  $\mathbf{l}$  is the vector along the direction from site  $m$  to site  $m+1$ . At this TI, an initial wave state, for example, marked by the green dot on the red band, experiences a vertical transition to the final state marked by the yellow dot on the violet band as shown in Fig. 1e, with the conservation of the momentum  $k$  and the change of the group velocity. In particular, if  $\Delta\varphi = \pi$ , such transition corresponds to a time reversal operation<sup>16</sup>. Before we end this section, we note that such two types of TIs can be combined together so one can perform the band-folding/band-unfolding and band-shifting operations simultaneously.

**Temporal non-Abelian AB interference in 2D gauge field**

With the two types of TIs introduced in the previous section, we now construct a temporal multilayer structure with three TIs which are operated at  $t = 6, 30, 54 \text{ g}^{-1}$ , respectively (Fig. 2a). At the first TI, we apply the band-unfolding operation which changes the system's Hamiltonian from  $H_2$  to  $H_1$  with  $\varphi = 0$ . The initial wave state  $(\omega, k)$  marked by the green dots in Fig. 2a projects onto two wave states  $(\omega_{1,2}, k_{1,2})$  marked by the yellow dots with different group velocities, and hence the initial wave packet splits into two parts with different propagation directions as shown in Fig. 2b. At the second TI at  $t = 30 \text{ g}^{-1}$ , we shift the coupling phase  $\varphi$  from 0 to  $\pi$  corresponding to a time reversal operation which changes the signs of group velocities of the two wave packets to the opposite ones. Then two wave states  $(\omega_1, k_1)$  and  $(\omega_2, k_2)$  project onto two new wave states  $(-\omega_1, k_1)$  and  $(-\omega_2, k_2)$ , respectively. At the same time, we add an additional phase  $\theta$  (i.e., phase shift operation) onto the  $k_1$  mode (details are given in "Methods" section). Lastly, at the third TI when the two wave packets encounter, we apply the band-folding operation and shift the coupling phase  $\varphi$  from  $\pi$  back to 0 simultaneously (detailed boundary conditions in temporal operations used in simulations are given in Methods). The two wave states  $(-\omega_1, k_1)$  and  $(-\omega_2, k_2)$  both project onto the state  $(\omega, k)$  with interference. However, there is the added phase difference  $\theta$  in two temporal paths, the combined wave state at the third TI may not return to the initial one. Such a temporal interference process between two degenerate states (i.e., the odd-distributed and even-distributed modes) can be described by the input-output relation

$$\begin{pmatrix} O_o \\ O_e \end{pmatrix} = \frac{1}{2} \begin{pmatrix} 1 & 1 \\ 1 & -1 \end{pmatrix} \begin{pmatrix} e^{i\theta} & 0 \\ 0 & 1 \end{pmatrix} \begin{pmatrix} 1 & 1 \\ 1 & -1 \end{pmatrix} \begin{pmatrix} I_o \\ I_e \end{pmatrix} = e^{i\theta/2} \begin{pmatrix} \cos(\theta/2) & i \sin(\theta/2) \\ i \sin(\theta/2) & \cos(\theta/2) \end{pmatrix} \begin{pmatrix} I_o \\ I_e \end{pmatrix}, \tag{7}$$

where  $(O_o, O_e)^T$  denotes the output state in the odd/even-distributed mode basis. We give a specific example with the numerical simulation in Fig. 2b by preparing the initial wave as a pure odd-distributed mode  $(I_o, I_e)^T = (1, 0)^T$  and choose  $\theta = 0.5\pi$  in the phase shift operation. The output wave can be predicted by Eq. (7), and the detailed evolution process is summarized in Fig. 2c, d where evolutions of odd number sites and even number sites are plotted separately. One can find the emergence of the even-distributed mode after the third TI ( $t > 54 \text{ g}^{-1}$ ) in Fig. 2d which shares the same intensity as that of the odd-distributed mode. Therefore, we here show a temporal interference in a temporal multilayer structure that offers us the opportunity to explore non-Abelian physics<sup>29,37-39</sup> which requires the transition between the internal degenerate states of a system.

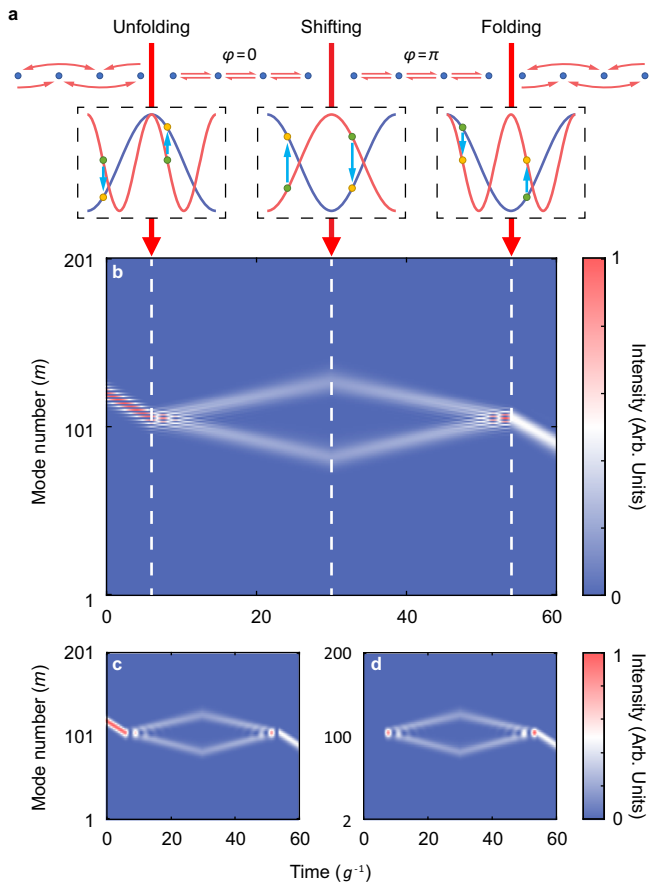


**Fig. 2 | Temporal interference of degenerate state.** **a** Lattice structures at different time intervals and changes of the band structure and states at different TIs, accordingly. Green (yellow) dots denote the states before (after) the TI. Blue arrows denote the change at the TI. **b** Evolution of the intensity distributions of the wave packet in the proposed temporal multilayer structure. The additional phase  $\theta$  is taken as  $\theta = 0.5\pi$ . **c, d** Evolutions of the intensity distribution only for odd number sites and even number sites, respectively. Arb. Units arbitrary units.

Before we explore the signatures of the non-Abelian AB interference, let us briefly review the non-Abelian AB interference in a two-dimensional (2D) gauge field<sup>30–33</sup>. If we consider a particle with pseudospin under a gauge field  $\mathcal{A}$ , which is described by

$$\mathcal{A} = A_x \mathbf{e}_x + A_z \mathbf{e}_z, \tag{8}$$

where  $\mathbf{e}_x$  and  $\mathbf{e}_z$  are the vectors along  $x$  and  $z$  direction in the parameter space, respectively. Suppose there are two paths with equal distance  $L$  along  $x$  and  $z$  direction for the particle to move from point A to point B as depicted in Fig. 3a.

The initial state of the particle  $\Psi_i$  and the final state  $\Psi_f$  can be linked by an operation  $U_\gamma$ , which is written by<sup>38</sup>

$$U_\gamma = \mathcal{P} \left[ \exp \left( i \int_\gamma \mathcal{A} \cdot d\mathbf{l} \right) \right], \tag{9}$$

where  $\gamma$  is a specific path and  $\mathcal{P}$  denotes a path-ordered integral, indicating that  $\Psi_f$  may depend on which path the particle chooses. If the particle first travels along  $x$  direction and then  $z$  direction, the final state is given by  $\Psi_f = \exp(iA_z L) \exp(iA_x L) \Psi_i$ . If the particle chooses the path first along  $z$  direction and then  $x$  direction, the final state is given by  $\Psi_f = \exp(iA_x L) \exp(iA_z L) \Psi_i$ . If  $\mathcal{A}$  is a non-Abelian gauge field,  $A_x$  and  $A_z$  do not commute and  $\Psi_f$  will be different depending on which

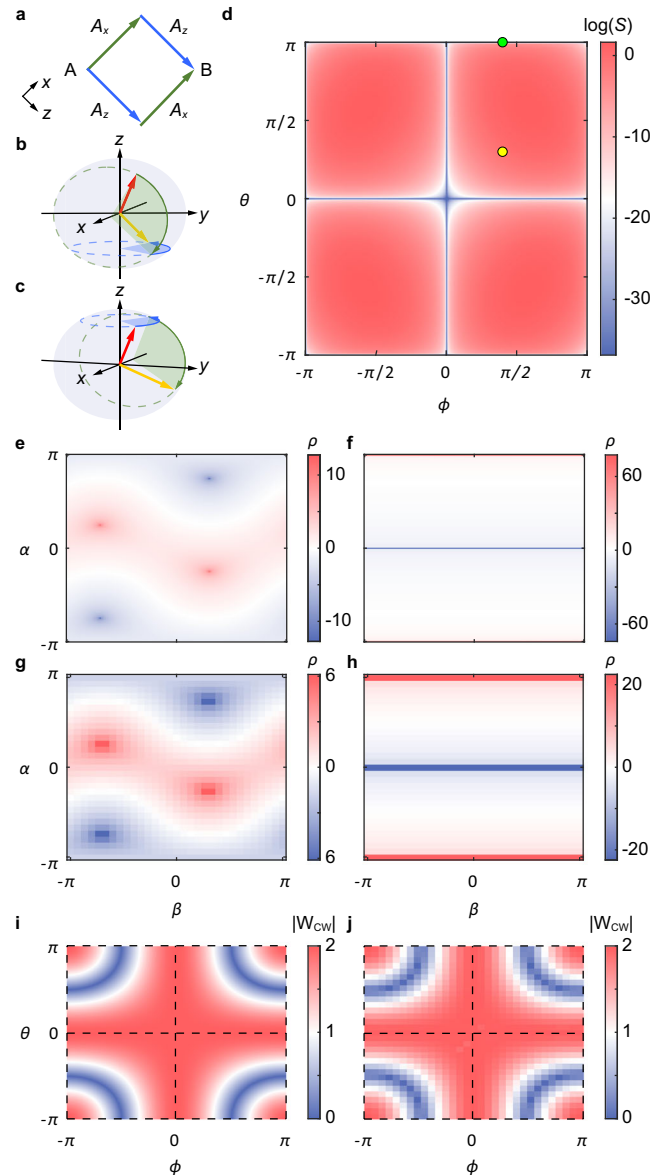


**Fig. 3 | Temporal AB interference and Wilson loop calculation in a 2D gauge field.** **a** Schematic of two paths for a particle moving from point A to point B under a gauge field  $\mathcal{A}$ . **b, c** Evolutions of the state vector of a particle following the two paths under a non-Abelian gauge field in the Bloch sphere. The red (yellow) arrow denotes the initial state (final state). **d** Plot of the logarithm of  $S$  versus parameters of the applied gauge field  $\phi$  and  $\theta$ , which shows whether the corresponding gauge field is Abelian (blue lines at  $\theta = 0, \pm\pi$  or  $\phi = 0, \pm\pi$ ) or non-Abelian. **e** Theoretical calculation and **g** numerical calculation results of the intensity contrast  $\rho$  between the two degenerate states after the interference versus initial intensity distribution  $\alpha$  and phase difference  $\beta$  under the non-Abelian interference. **f, h** Theoretical calculation and numerical calculation results of  $\rho$  under the Abelian interference. **i** Theoretical calculation and **j** numerical simulation results of the Wilson loop  $|W_{CW}|$ , where  $|W_{CW}| \neq 2$  is a necessary but insufficient condition for a non-Abelian gauge field. Black dash lines indicate the genuine non-Abelian cases.

path the particle takes. We make an illustration of the evolution of the particle for the two paths in the Bloch sphere as shown in Fig. 3b, c by taking  $A_x L \propto \sigma_x$  and  $A_z L \propto \sigma_z$ , where  $\sigma_x$  and  $\sigma_z$  are the Pauli matrices. The non-Abelian gauge field results in sequential rotations of the state vector around two different axes. One can find that although the system starts with the same initial state  $\Psi_i$  (red arrows in Fig. 3b, c), it ends in different final states  $\Psi_f$  (yellow arrows in Fig. 3b, c). The non-

Abelian AB interference corresponds to the interference of these two different final states in such a non-Abelian gauge field.

Now we finally illustrated the way in constructing the non-Abelian AB interference occurs with the temporal multilayer structure in Fig. 2a and the resulting signatures for observing such temporal interference presented in Fig. 3e–j. We first show how to realize the two non-commutable operations in the temporal domain, which is the key to emulating non-Abelian AB interference. The temporal degenerate-state interference previously discussed in Fig. 2a can be represented as an operation  $U_\theta = e^{i\theta\sigma_x}$ , which can be used to simulate the  $\sigma_x$  gauge field. To construct the relevant  $\sigma_z$  gauge field, we apply the phase shift operation on the even-distributed mode with the phase  $\phi$ , which can be represented by the operation  $U_\phi = e^{i\phi\sigma_z}$ . With the two temporal operations on-hand, we show the temporal version of the non-Abelian AB interference under the gauge field in Fig. 3a. Firstly, we perform the  $U_\theta$  operation and then the  $U_\phi$  operation at  $t = 57\text{g}^{-1}$  to obtain a final state  $\Psi_f^{\theta\phi} = e^{-i\theta\sigma_z} e^{i\phi\sigma_x} \Psi_i$  with the global phase being neglected (details are shown in the supplementary material Section II), which corresponds to the state vector sequentially rotates around the  $x$  and  $z$  axis in Fig. 3b. Similarly, we can obtain a final state  $\Psi_f^{\phi\theta} = e^{i\phi\sigma_x} e^{-i\theta\sigma_z} \Psi_i$  by performing the  $U_\phi$  operation at  $t = 3\text{g}^{-1}$  with a followed  $U_\theta$  operation, which corresponds to the sequential rotation of state vector around the  $z$  and  $x$  axis in Fig. 3c. Such two sequential operations can be performed simultaneously so the resulting interference pattern  $\Psi_{\text{inter}} = \Psi_f^{\theta\phi} + \Psi_f^{\phi\theta} = (\psi_1, \psi_2)^T$  can be reached. Constructing other forms of non-Abelian gauge field needs a cascade of the two operations described above. By engineering other kinds of TIs, one may possibly generate the desired non-Abelian gauge field independently.

We now study the choices of values of  $\theta$  and  $\phi$  that can synthesize a non-Abelian gauge field. The criterion of a genuine non-Abelian gauge field is the non-commutativity of two holonomies<sup>38</sup>. Here we choose a pair of time-reversal operations  $U_{\text{CW}}$  and  $U_{\text{CCW}}$  which start and end at point A in Fig. 3a defined as<sup>32</sup>

$$U_{\text{CW}} \equiv \mathcal{P} \left[ \exp \left( i \oint_{\text{CW}} \mathbf{A} \cdot d\mathbf{l} \right) \right] = e^{i\theta\sigma_z} e^{-i\phi\sigma_x} e^{-i\theta\sigma_z} e^{i\phi\sigma_x}, \quad (10)$$

and

$$U_{\text{CCW}} \equiv \mathcal{P} \left[ \exp \left( i \oint_{\text{CCW}} -\mathbf{A} \cdot d\mathbf{l} \right) \right] = e^{i\phi\sigma_x} e^{-i\theta\sigma_z} e^{-i\phi\sigma_x} e^{i\theta\sigma_z}, \quad (11)$$

respectively. We plot the logarithm of the summation  $S = \sum_{a,b} |[U_{\text{CW}}, U_{\text{CCW}}]_{ab}|^2$  as the phase diagram in Fig. 3d, where  $[U_{\text{CW}}, U_{\text{CCW}}]_{ab}$  is the element at the  $a$ -th row and the  $b$ -th column of the commutation  $[U_{\text{CW}}, U_{\text{CCW}}]$ . At  $\phi = 0, \pm\pi$  and  $\theta = 0, \pm\pi$ , one can see  $[U_{\text{CW}}, U_{\text{CCW}}] = 0$ , indicating the Abelian case, while at other choices of  $\phi$  and  $\theta$ ,  $[U_{\text{CW}}, U_{\text{CCW}}] \neq 0$ , corresponding to the non-Abelian case. The Abelian case with  $\theta = 0$  or  $\phi = 0$  can be easily understood, as the state vector only rotates around the  $x$  or  $z$  axis through the whole holonomy, and therefore the two operations  $U_{\text{CW}}$  and  $U_{\text{CCW}}$  are commutable, while the Abelian cases with  $\theta = \pm\pi$  or  $\phi = \pm\pi$  cases are special since the state vector rotates around both the  $x$  and  $z$  axis, but the two operations are still commutable.

The non-Abelian AB interferences are explored in Fig. 3e, g, with comparisons from their Abelian counterparts in Fig. 3f, h. In detail, we prepare the initial state by  $\Psi_i(\alpha, \beta) = (\cos \alpha/2, e^{i\beta} \sin \alpha/2)$  with parameters  $\alpha, \beta \in [-\pi, \pi]$ . Here,  $\alpha$  denotes the intensity distribution between the two degenerate states, and  $\beta$  denotes the phase difference between them. The intensity contrast is defined as

$$\rho = \log(|\psi_1|^2 / |\psi_2|^2), \quad (12)$$

which are calculated both theoretically and numerically to present the interference pattern  $\Psi_{\text{inter}}$ . We plot theoretical results of a non-Abelian case in Fig. 3e with  $\theta = 0.3\pi$  and  $\phi = 0.4\pi$ , as well as an Abelian one in Fig. 3f with  $\theta = \pi$  and  $\phi = 0.4\pi$ , which are depicted as the yellow and green dots respectively in the phase diagram in Fig. 3d. The choice of these parameters supports a general case of an Abelian (non-Abelian) AB interference. For the non-Abelian case in Fig. 3e  $\rho$  varies with both the intensity distribution  $\alpha$  and the phase difference  $\beta$ , indicating a mixture between the two degenerate states, and hence reflecting the non-Abelian nature of the gauge field. Moreover, we can see that poles emerge at specific choices of  $(\alpha, \beta) = (0.25\pi, -0.7\pi), (-0.25\pi, 0.3\pi), (-0.75\pi, -0.7\pi)$  and  $(0.75\pi, 0.3\pi)$  where the even-distributed or odd-distributed modes of  $\Psi_f^{\theta\phi}$  and  $\Psi_f^{\phi\theta}$  take destructive interference. For the Abelian case, as  $\theta = \pi$  which causes a switching rather than a mixture between the two degenerate states, the phase difference  $\beta$  of the initial state has no effect on the interference (Fig. 3e). As a result, the intensity contrast  $\rho$  only varies with the distribution  $\alpha$  of the initial state. We also perform numerical simulations to verify our theoretical calculations (where detailed numerical procedure can be found in the supplementary material Section II) and plot numerical results in Fig. 3g, h, which are well consistent with the theoretical results in Fig. 3e, f.

Another criterion of the existence of a non-Abelian gauge field is the Wilson loop  $W = \text{Tr}(U_C)^{38}$ , where  $U_C$  is the Berry holonomy. For an  $N$ -dimensional loop operation  $U_C$ ,  $|W| = N$  points to the case of the Abelian gauge field. Here we calculate the theoretical result of the Wilson loop in the proposed temporal multilayer structure by taking  $|W_{\text{CW}}| = |\text{Tr}(U_{\text{CW}})|$  versus  $\theta$  and  $\phi$  and plot it in Fig. 3i. Compared with the phase diagram in Fig. 3d, one sees that the results of  $|W_{\text{CW}}| = 2$  in Fig. 3i and  $[U_{\text{CW}}, U_{\text{CCW}}] = 0$  in Fig. 3d are matched well at  $\theta = 0$  or  $\phi = 0$ , while they are inconsistent in the vicinity of  $\theta = \pm\pi$  or  $\phi = \pm\pi$ . The reason is that  $|W| \neq 2$  is a necessary but insufficient condition for the presence of a non-Abelian gauge field<sup>38</sup>. We also perform the numerical simulation to extract  $|W_{\text{CW}}|$  plotted in Fig. 3j, which also shows good agreement with the theoretical result in Fig. 3i.

### Towards interference in higher-dimensional gauge field

It is of fundamental interest in exploring non-Abelian gauge fields in higher dimensions ( $N > 2$ ). However, to do so, an  $N$ -fold degenerate state is required as the key ingredient, which is intrinsically challenging in previous atomic or photonic platforms<sup>27,32,40–43</sup> due to the limitation of the degenerate modes in nature. One advantage of the proposed temporal multilayer structure is the capability for constructing an arbitrary  $N$ -fold degenerate state. Therefore, in this section, we showcase an example of the temporal non-Abelian AB interference in a three-dimensional gauge field, and point out the possibility in generalizing towards higher dimensions.

We here consider a third lattice Hamiltonian

$$H_3 = g \sum_m (e^{-i\phi} a_m^\dagger a_{m+3} + e^{i\phi} a_{m+3}^\dagger a_m), \quad (13)$$

that supports the next-next-nearest neighbor couplings. The model of  $H_3$  can be splitted into three independent subsystems, which therefore the system supports a trifold degenerate state for given  $\omega'$  and  $k'$  with  $k' = k'_0 + 2r\pi/3l$ , where  $k'_0 \in [-\pi/3l, \pi/3l]$ . The trifold degenerate eigenstates can be written into mode site basis with  $(\psi'_1, \psi'_2, \psi'_3) = (1, 0, 0)^T, (0, 1, 0)^T$  and  $(0, 0, 1)^T$  where  $\psi'_i$  represent the  $(3n+i)$ -th sites with  $n$  and  $i$  being integers. After performing a similar band-unfolding operation by converting  $H_3$  into  $H_1$ , states project into three eigenstates with different momentum, denoted by  $(\omega'_1, k'_1), (\omega'_2, k'_2)$  and  $(\omega'_3, k'_3)$  with  $k'_1 = k'_0 + 2r\pi/l, k'_2 = k'_1 + 2\pi/3l$  and  $k'_3 = k'_1 + 4\pi/3l$ , respectively. The noncommutative operations  $U'_{\theta_1, \theta_2}$  and  $U'_{\phi_1, \phi_2}$  can be achieved by a similar manner as the twofold case,

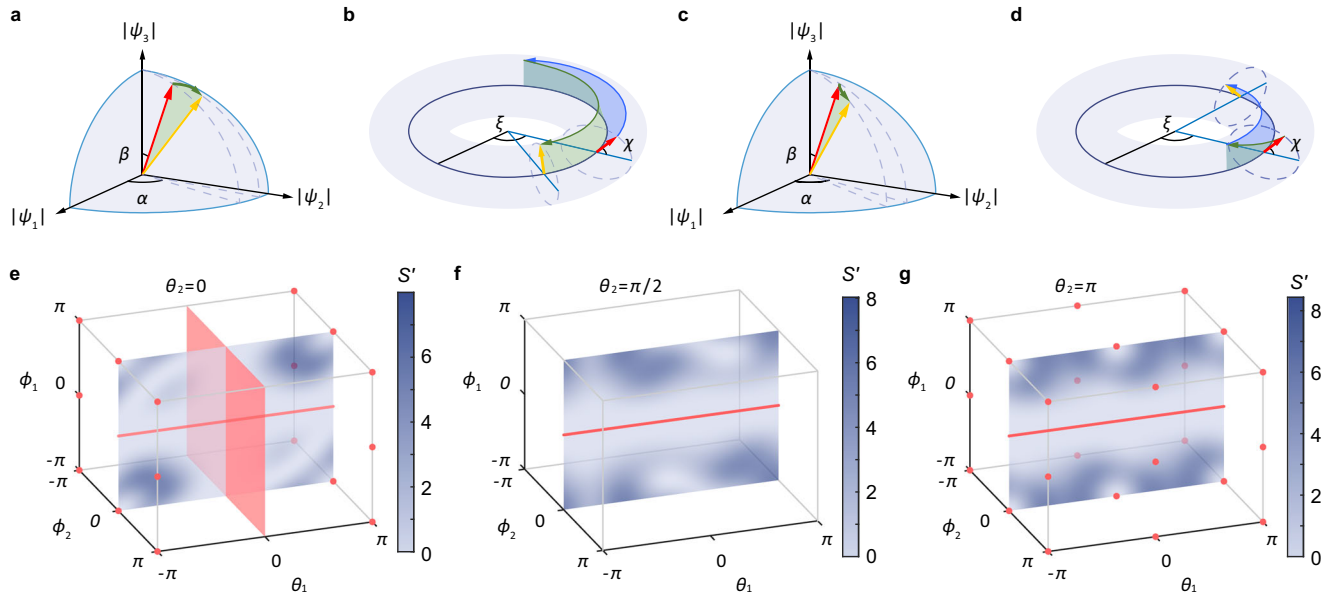


**Fig. 4 | Extension to a three-dimensional gauge field.** **a, b** Evolutions of the state vector in the parameter space with two sequential operations  $U'_{\theta_1, \theta_2}$  and  $U'_{\phi_1, \phi_2}$ . **c, d** Evolutions of the state vector in the parameter space with two sequential operations  $U'_{\phi_1, \phi_2}$  and  $U'_{\theta_1, \theta_2}$ . Red (yellow) arrows denote the initial state  $\Psi_i$  (final state  $\Psi_f$ ). **e–g** Theoretical calculation results of commutation of the two evolution

operators  $[U_{CW}, U_{CCW}]$  versus parameters of the applied gauge field  $\theta_1, \phi_1$  and  $\phi_2$  for **e**  $\theta_2 = 0$ , **f**  $\theta_2 = \pi/2$ , and **g**  $\theta_2 = \pi$ , respectively. The red dots, lines, and surface represent regions where  $[U_{CW}, U_{CCW}] = 0$  (i.e., an Abelian gauge field). The color-maps are the slices of  $S'$ , where  $S' \neq 0$  represents the genuine non-Abelian cases.

where

$$U'_{\theta_1, \theta_2} = \frac{1}{3} \begin{pmatrix} 1 & 1 & 1 \\ 1 & e^{i2\pi/3} & e^{-i2\pi/3} \\ 1 & e^{-i2\pi/3} & e^{i2\pi/3} \end{pmatrix} \begin{pmatrix} e^{i\theta_1} & 0 & 0 \\ 0 & e^{i\theta_2} & 0 \\ 0 & 0 & 1 \end{pmatrix} \begin{pmatrix} 1 & 1 & 1 \\ 1 & e^{-i2\pi/3} & e^{i2\pi/3} \\ 1 & e^{i2\pi/3} & e^{-i2\pi/3} \end{pmatrix} \quad (14)$$

is realized by a band-unfolding operation followed by a time reversal operation as well as phase shift operations  $\theta_1$  and  $\theta_2$  for modes  $(\omega_1, k'_1)$  and  $(\omega_2, k'_2)$  respectively, and finally a band-folding operation;

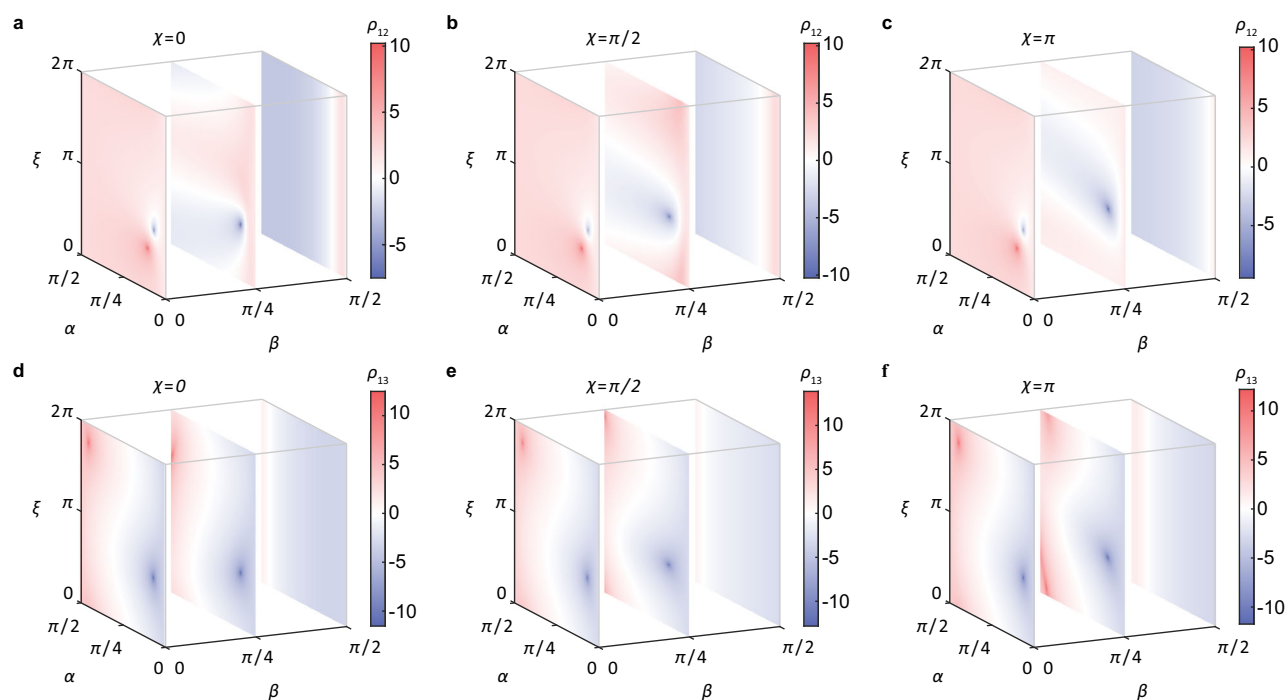
$$U'_{\phi_1, \phi_2} = \begin{pmatrix} e^{i\phi_1} & 0 & 0 \\ 0 & e^{i\phi_2} & 0 \\ 0 & 0 & 1 \end{pmatrix} \quad (15)$$

is realized by phase shifts  $\phi_1$  and  $\phi_2$  to  $\psi'_1$  and  $\psi'_2$  in  $H_3$ . With these two operations, we can construct the same configuration of non-Abelian gauge field  $A' = A'_x \mathbf{e}_x + A'_z \mathbf{e}_z$  as shown in Fig. 3a.  $A'_x$  and  $A'_z$  are linked with  $U'_{\theta_1, \theta_2}$  and  $U'_{\phi_1, \phi_2}$  by  $U'_{\theta_1, \theta_2} = \exp(iA'_x L)$  and  $U'_{\phi_1, \phi_2} = \exp(iA'_z L)$ . We then perform the non-commutativity of the two operations. The wave state  $\Psi(\psi'_1, \psi'_2, \psi'_3)$  can be parametrized by  $\Psi(\alpha, \beta, \xi, \chi) = (e^{i\xi} \cos(\alpha) \sin(\beta), e^{i\chi} \sin(\alpha) \sin(\beta), \cos(\beta))^T$ , where  $\alpha, \beta \in [0, \pi/2]$  and  $\xi, \chi \in [0, 2\pi]^{44}$ . Here,  $\alpha, \beta$  denotes the intensity distribution between the degenerate states, and  $\xi, \chi$  denotes the phase differences between them. These four parameters thus span a four-dimensional parameter space, which can be represented by the direct product of two 2D surfaces, i.e., an octant  $(\alpha, \beta)$  and a torus  $(\xi, \chi)$  shown in Fig. 4a, b. Any pure state can be viewed as a point on the two surfaces respectively. We choose an initial state  $\Psi_i$ , and then successively implement operations  $U'_{\theta_1, \theta_2}$  and  $U'_{\phi_1, \phi_2}$  or  $U'_{\phi_1, \phi_2}$  and  $U'_{\theta_1, \theta_2}$ . The trajectories of state vector in the parameter space are shown in Fig. 4a–d, where green (blue) arrow lines denote the action of  $U'_{\theta_1, \theta_2}$  ( $U'_{\phi_1, \phi_2}$ ) to the state vector. One can find that  $U'_{\phi_1, \phi_2}$  has no effect on the octant  $(\alpha, \beta)$  as it only changes the phase differences  $\xi$  and  $\chi$ , while  $U'_{\theta_1, \theta_2}$  change the state vector in both the octant  $(\alpha, \beta)$  and the torus  $(\xi, \chi)$ . Moreover, the two operations  $U'_{\theta_1, \theta_2}$  and  $U'_{\phi_1, \phi_2}$  show non-commutativity in Fig. 4a–d, implying that  $A'_x$  and  $A'_z$  are not commutable. In Fig. 4e–g, the results of

$[U_{CW}, U_{CCW}]$  are shown. The red dots, lines and surface represent regions where  $[U_{CW}, U_{CCW}] = 0$  (i.e., an Abelian gauge field). Apart from the common Abelian cases being denoted by the red lines and surface where only one type operation is taken on  $\Psi$  actually (i.e., either  $\phi_1$  and  $\phi_2$  or  $\theta_1$  and  $\theta_2$  take 0), the special Abelian cases being denoted by red dots appear in Fig. 4e, g but not in Fig. 4f for the reason that  $U'_{\theta_1, \theta_2}$  is noncommutative with  $U'_{\phi_1, \phi_2}$  except for  $(\phi_1, \phi_2) = (0, 0)$ . Therefore we can conclude that the condition for a special Abelian case is  $\theta_1, \theta_2, \phi_1$ , and  $\phi_2$  take the value 0 or  $\pm \pi$  with  $(|\theta_1| + |\theta_2|)(|\phi_1| + |\phi_2|) \neq 0$ . We also show the slices of  $S' = \sum_{a,b} |[U_{CW}, U_{CCW}]_{ab}|$  in Fig. 4e–g. One can find that the patterns of  $S'$  display a central symmetry at  $(\phi_1, \phi_2, \theta_1) = (0, 0, 0)$  in Fig. 4e, g, while the center of symmetry of the pattern in Fig. 4f seems to be shifted along  $\theta_1$  direction.

We then perform the AB interference under a trifold non-Abelian gauge field with  $\theta_1 = 0.3\pi$ ,  $\theta_2 = 0.4\pi$ ,  $\phi_1 = 0.7\pi$ , and  $\phi_2 = 1.2\pi$  to give an example of a general case of the consequence of such a high-dimensional non-Abelian gauge field. The theoretical results of intensity contrast  $\rho_{12}$  and  $\rho_{13}$  which are defined as  $\rho_{ij} = \log(|\psi_i|^2 / |\psi_j|^2)$  with various initial state  $\Psi_i(\alpha, \beta, \xi, \chi)$  are shown in Fig. 5a–c and d–f, respectively. The interference patterns again vary with not only the intensity distribution  $\alpha$  and  $\beta$ , but also the phase differences  $\xi$  and  $\chi$ , which reflects the non-Abelian nature of the mixing between the degenerate states. Moreover, one finds that not only the strip-like patterns in Fig. 5d–f similar to the twofold case in Fig. 3e, but also more complex patterns in Fig. 5a–c are displayed. This may indicate that there are exotic phenomena lying on a higher dimensional gauge field. We also show the simulation results of  $\rho_{ij}$  by numerically solving the temporal multilayer structure with a similar approach of the twofold case in Fig. 5g–i, which consists quite well with the theoretical ones. We further plot the theoretical and numerical results of the Wilson loop  $|W_{CW}|$  in Fig. 6 with  $\theta_1, \theta_2, \phi_1$ , and  $\phi_2$  varying, which gives good agreement between each other. Furthermore, one can find that the regions of  $|W_{CW}| = 3$  correspond to the common Abelian case by comparing Figs. 4e–g and 6. For example, the red region near  $\theta_1 = 0$  in Fig. 6a always exists along  $\phi_1$  direction, which corresponds to the red surface in Fig. 4e, but the red region near  $\phi_1 = 0$  along  $\theta_1$  direction only exists for  $\phi_2 = 0$  in all three cases in Fig. 6 which correspond to the red

Theoretical calculation:



Numerical simulation:

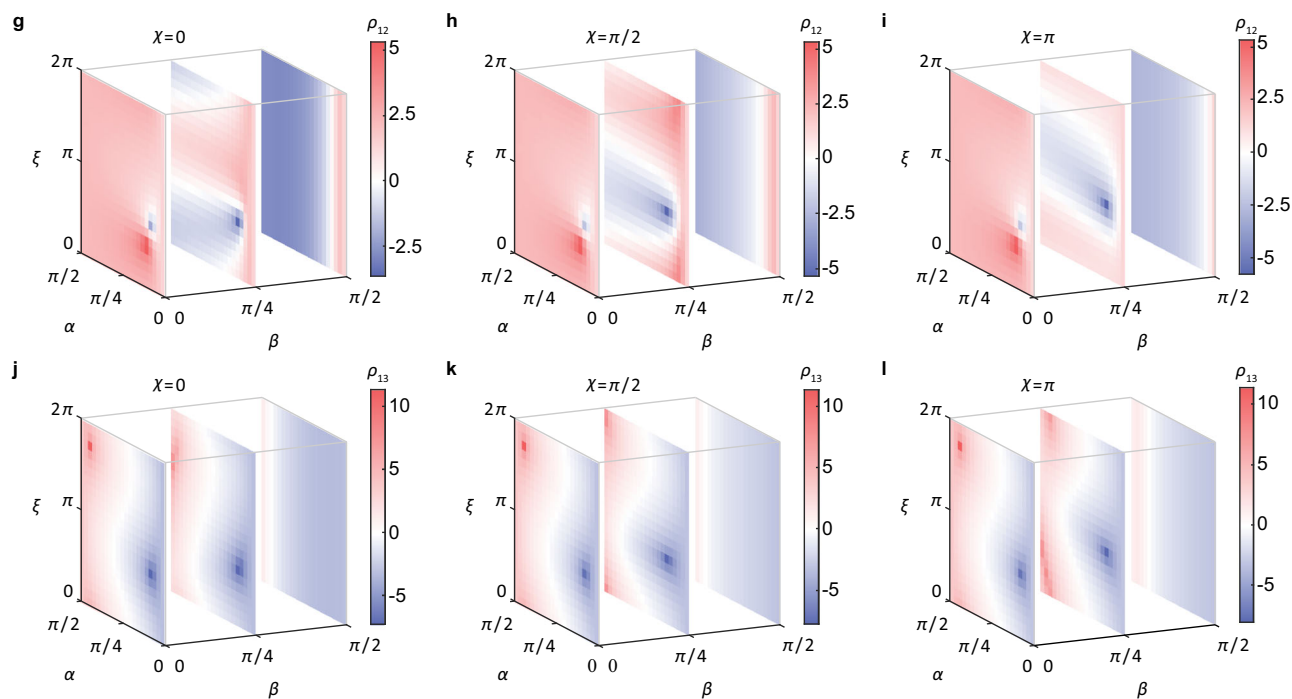


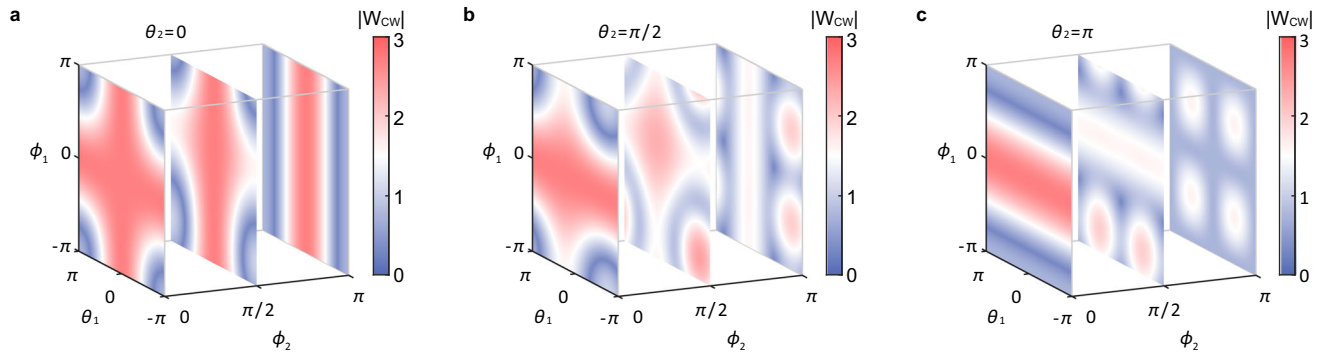
**Fig. 5 | Temporal non-Abelian AB interference in a three-dimensional gauge field.** Theoretical calculation results of the intensity contrast **a–c**  $\rho_{12}$  and **d–f**  $\rho_{13}$  between the degenerate states after the non-Abelian interference versus

parameters initial intensity distribution  $\alpha$ ,  $\beta$  and phase differences  $\xi$  for  $\chi=0, \pi/2$ , and  $\pi$ , respectively. Numerical simulation results of the intensity contrast **g–i**  $\rho_{12}$  and **j–l**  $\rho_{13}$  versus parameters  $\alpha$ ,  $\beta$  and  $\xi$  for  $\chi=0, \pi/2$ , and  $\pi$ , respectively.

lines in Fig. 4e–g. Furthermore, one can find that  $|W_{\text{CW}}| \neq 3$  for the points of the special Abelian cases (see the corners of the figures). These again show the necessity but insufficiency of the Wilson loop criterion. We want to point out that the presented temporal multilayer

structure can only simulate specific types of three-dimensional non-Abelian gauge fields because of the limited number of parameters. As the operation  $U \in \text{SU}(3)$  under an arbitrary three-dimensional non-Abelian gauge field is characterized by eight independent

Theoretical calculation:



Numerical simulation:

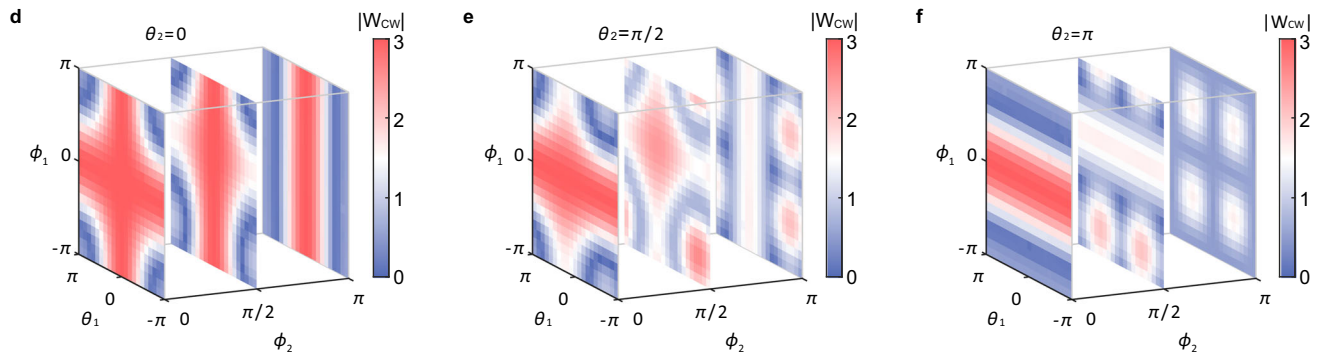


**Fig. 6 | Wilson loop calculation of a three-dimensional gauge field.**

**a–c** Theoretical calculation and **d–f** numerical simulation results of the Wilson loop  $|W_{CW}|$  versus parameters of the applied gauge field  $\theta_1, \theta_2, \phi_1,$  and  $\phi_2$  for  $\theta_2 = 0, \pi/2,$

and  $\pi$ , respectively. Here,  $|W_{CW}| \neq 3$  is a necessary but insufficient condition for a non-Abelian gauge field.

parameters<sup>45</sup>, while there are only four parameters in our model. However, an arbitrary operation  $U \in \text{SU}(3)$  may also be possibly achieved by sequential operations  $U'_{\phi_1, \phi_2} U'_{\theta_1, \theta_2} U'_{\phi_1, \phi_2} U'_{\theta_1, \theta_2}$  where eight independent parameters are included (see the supplementary material Section III).

Before ending this section, we discuss the potential generalization to a higher-dimensional gauge field in our proposal. We introduce a model with the Hamiltonian

$$H_N = g \sum_m (e^{-i\varphi} a_m^\dagger a_{m+N} + e^{i\varphi} a_{m+N}^\dagger a_m). \quad (16)$$

We can again split  $H_N$  into  $N$  independent subsystems, and therefore such a lattice model can support an  $N$ -fold degenerate state. Band unfolding/folding and phase shift operations may also be applied with the temporal multilayer structure. An  $N$ -dimensional non-Abelian gauge field can be constructed by a similar manner as the procedure similar to the twofold and trifold cases. The temporal multilayer structure cooperating with phase shift operations can generate rotations of the state vector around two non-parallel axes, which correspond to two noncommutative operations for the state and therefore realize two noncommutative gauge field components. Further AB interference under an  $N$ -dimensional non-Abelian gauge field may also be demonstrated.

### Possible experimental implementations

We have shown the in-principle capability for the proposed temporal multilayer structure to create  $N$ -dimensional non-Abelian gauge fields in a space including the time dimension. Here in this section, we further discuss possible experimental implementations for achieving

such a proposal, as well as the potential outputs in future experiments. Although our proposal desires several flexible operations in connecting discrete sites with required hopping phases, it can be potentially realized in various kinds of discrete physical systems, ranging from real space to synthetic dimension. In real space, waveguide arrays<sup>46,47</sup> and coupled-resonator optical waveguides<sup>48</sup> could be potential candidates for the proposed temporal multilayer structure. Spatial discrete photonic crystal models may also be possible as long as one can apply all desired operations at different times<sup>1–4,49,50</sup>. Recent developed synthetic dimensions in photonics<sup>51–55</sup> such as time-bins<sup>17,20,35,56–58</sup> and frequency lattice<sup>59–65</sup> also provide a convenient way to fulfill these tasks. Here, as a pedagogical example, we take the toy model in the synthetic frequency dimension<sup>59–65</sup>, which leverages the discrete resonant frequency modes of light as the sites in synthetic space. With appropriate external modulations<sup>61–65</sup>, the connectivities between resonant modes can be designed, which provide desired operations and Hamiltonians. In the following, we take the twofold case as an example to explicitly illustrate the possible experimental implementation with the synthetic frequency dimension. As a side note, we also give a brief discussion on the possible implementations for other experimental platforms such as time bins, waveguide arrays, and coupled-resonator optical waveguides in the supplementary material Section IV.

The scheme of our proposal is shown in Fig. 7a, where light circulates inside a ring resonator with zero group velocity dispersion, supporting resonant modes at frequencies  $\omega_p = \omega_0 + p\Omega$ . Here  $\omega_0$  is the reference frequency,  $\Omega$  is the frequency spacing between two nearby modes, and  $p$  is an integer. The resonator is dynamically modulated by an electro-optic modulator (EOM) with the phase modulation  $\Gamma = \exp[i\kappa \cos(q\Omega t + \varphi_m)]$ , where  $\kappa \ll 1$  is the modulation strength,  $q\Omega$  is the modulation frequency ( $q$  is a positive integer) and  $\varphi_m$  is the

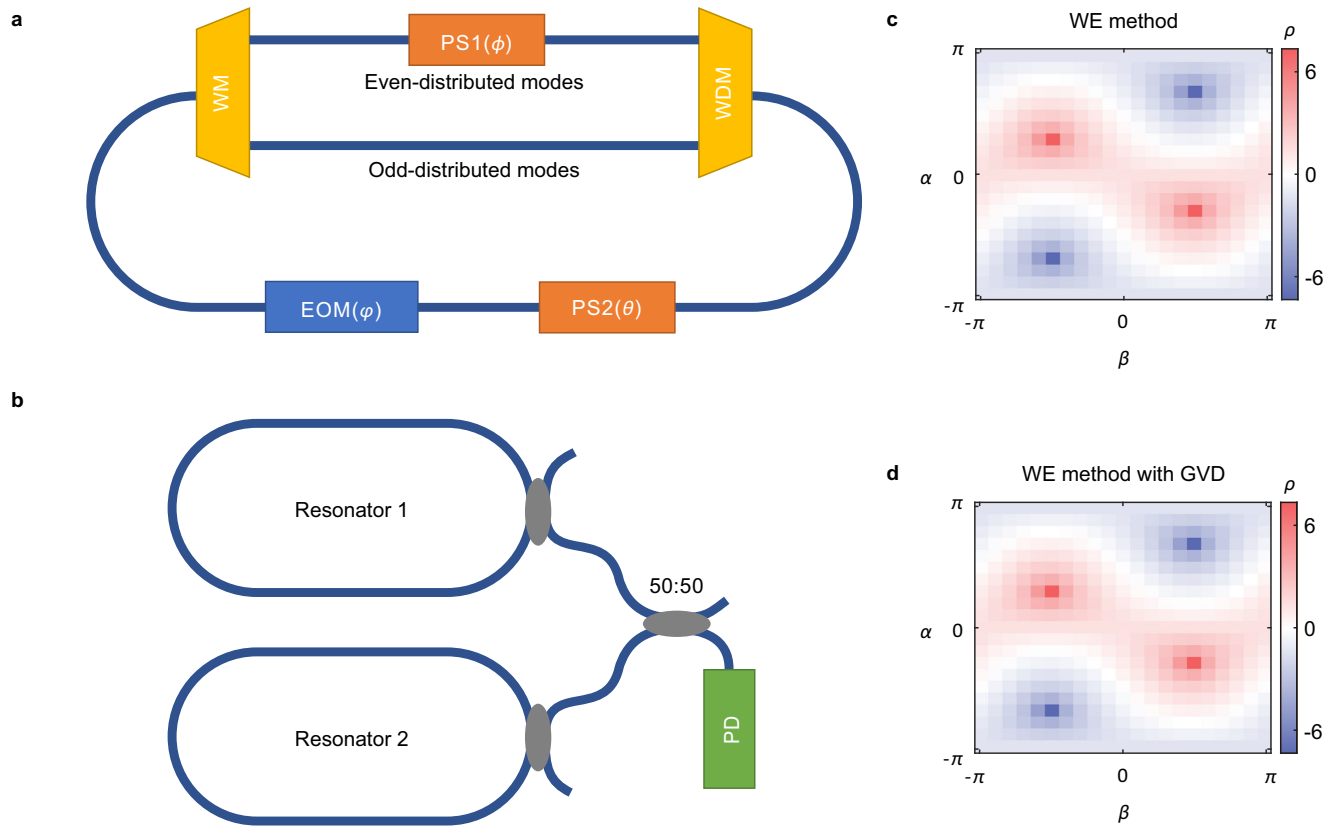


**Fig. 7 | Schematic of the possible experimental implementation proposal for achieving the proposed temporal multilayer structure and simulations based on WE method. a** A modulated ring resonator supports the synthetic frequency lattice model to realize the non-Abelian gauge field. **b** Scheme for measuring the non-Abelian AB interference using two such resonators. EOM electro-optic

modulator, PS1(2) phase shifter 1(2), WM wavelength multiplexer, WDM wavelength demultiplexer, 50:50 50:50 coupler, PD photodetector. **c, d** Numerical calculation results based on WE method of the intensity contrast  $\rho$  between the two degenerate states after the interference versus initial intensity distribution  $\alpha$  and phase difference  $\beta$  under the non-Abelian interference **c** without or **d** with GVD being included.

modulation phase. The coupling strengths and phases between lattice sites may vary with the number of resonances in principle. However, such variation could be neglected for the case we considered from rigorous theoretical analysis in ref. 59 and from recent experiments<sup>59,61–65</sup>, so the translational symmetry of the synthetic frequency lattice can hold. Such a scheme constructs a synthetic lattice with the site spacing  $q\Omega$  along the frequency axis of light<sup>59</sup>. In order to conduct a band-unfolding operation, i.e., turning the Hamiltonian  $H_2$  in Eq. (2) to  $H_1$  in Eq. (1), one can change the modulation frequency from  $2\Omega$  to  $\Omega$ <sup>60,61</sup>. A time reversal operation can be realized by tuning the modulation phase from  $\phi_m = 0$  to  $\phi_m = \pi$ . Moreover, a pair of wavelength demultiplexer (WDM) and wavelength multiplexer (WM) is used to separate even-distributed modes (even  $p$ ) and odd-distributed modes (odd  $p$ ) propagating into different paths (Fig. 7a)<sup>66</sup> while in the upper path there exists a phase shifter 1 (PS1) providing a phase shift  $\phi$ . In the modulated resonator supporting the synthetic frequency dimension, the circulating time inside the ring resonator gives the momentum that is reciprocal to the frequency<sup>59–62</sup>. Hence we place another phase shifter 2 (PS2) in the main path of the resonator, and if it is only turned on in the vicinity of the time corresponding to the momentum  $k_1$  for each roundtrip, a phase shift  $\theta$  can then be added onto the  $k_1$  mode. By conducting these operations in a proper time sequence, one can construct the temporal non-Abelian gauge field following the procedure of the temporal multilayer structure described in the previous section.

To observe the resulting non-Abelian AB interference, we use two configurations of ring resonators in Fig. 7a to produce two wave states  $\Psi_r^{\phi\theta}$  and  $\Psi_l^{\phi\theta}$  respectively (see Fig. 7b). Such two wave states are interfered at a 50:50 coupler via external waveguides and get detected

by the photodetector (PD). The key difference in the resulting intensity distributions from the output spectra at PD can therefore provide key potential experimental evidence between an Abelian AB interference and a non-Abelian one (see supplementary material Section V). For the Abelian case, the resulting intensity distribution is identical to the input field spectral distribution except for a shift of the envelope along the frequency axis, meaning that the phase difference  $\beta$  between the even-distributed and odd-distributed modes in the proposed system has no effect on the interference pattern. As a comparison, for the non-Abelian case, the resulting intensity distribution is different from the input one, with a clear interference pattern that varies with both  $\alpha$  and  $\beta$ .

To further demonstrate the confirmation of the adequacy for experimental situations, we introduce the rigorous numerical approach based on wave-equation (WE) method (see details in the supplementary material Section VI), which has been successfully proven as very useful in predicting/verifying experimental observations<sup>59,61–65</sup>. In Fig. 7c, d, we show numerical calculation results of the intensity contrast  $\rho$  based on WE method without (Fig. 7c) or with (Fig. 7d) the group velocity dispersion (GVD) being included. One can find that both simulation results based on WE method show a good agreement with the one based on the tight-binding Hamiltonian in Fig. 3g. Therefore, we can conclude that the effect of frequency-dependent dispersion is negligible for the experimental proposal in our considerations. We also discuss the effects of the presence of losses or noises in the supplementary material Section VII, where we find that the interference patterns still preserve under losses and coupling temporal noises. To evaluate the effect of the intracavity loss and noise which broaden the spectral linewidth of the resonant modes, we summarized the experimental characteristics of recent

experiments in synthetic frequency dimension<sup>62,63,67,68</sup> and find that the resonant modes can still be well distinguished with the presence of intracavity loss and noise (see the supplementary material Section VII). As for noises in the input field, the results can still be valid for small perturbations, but they may no longer be maintained if the disorder of the input field becomes too strong, because it causes a severe broadening of the input wave packet in the frequency or reciprocal space and then the two wave packets cannot be well separated after the band unfolding operation. Therefore, a high preparation fidelity of the input wave packet is essential to the experimental demonstration of our proposal, which can be achieved with the current photonic technology<sup>63</sup>. Moreover, the TI could be smooth in experiments. We analyze how the sharpness of the TI influences the interference, and conclude that the required operation speed for the modulation frequency and phase change can be loosened in the supplementary material Section VIII. Lastly, one should also notice that the scattering feature at a TI is different between a Maxwell's-equations-governed system and a Schrödinger-equation-governed system<sup>69,70</sup>. Such a difference should be taken into account for experimental realization in some platforms. All the simulation results in this work are performed without taking an analytical solution of the TIs.

### Discussion

In summary, we showcase the construction of the temporal multilayer structure with multiple functional TIs to support simulations of the two-/three-dimensional non-Abelian gauge field in the time domain. Discrete systems are modeled so one can perform flexible band engineerings at different times. The degenerate states in bandstructures are taken so noncommutative operations for the combined state with the time evolution can be designed to realize the non-Abelian AB interference. As the unique advantage, the proposed method provides a simple strategy to construct a high-dimensional degenerate space, and the noncommutative operations to realize non-Abelian AB interference are relatively straightforward, which enables the extension to arbitrary dimensional interference, especially when the synthetic dimension is used. Such a proposal may be potentially implemented in various discrete physical systems with the recently developed technology, including real space<sup>46-48</sup> and synthetic dimensions in photonics<sup>51-55</sup> as well as in atoms<sup>55,70</sup>.

At last, we want to emphasize that the studied temporal multilayer structure in discrete systems here holds unique features which have not been pointed out in previous works to the best of our knowledge. In particular, for a discrete system, the lattice structure can be flexibly tuned with reconfigurable long-range couplings and coupling phases, so it provides key ingredients for the realization of the non-Abelian gauge field with higher dimensions. The resulting arbitrary non-Abelian AB interference in the time domain is fundamentally important for deepening our understanding of non-Abelian physics and wave field manipulation in real and synthetic space. Therefore, our work may trigger further research interests in the temporal periodic structure in discrete systems including both spatial boundaries and TIs. Furthermore, the scattering features of TI in discrete systems are still largely unexplored, so further studies could enrich the building blocks to build more temporal multilayer structures with different functionalities. Lastly, the combination of spatial and temporal degrees of freedom can also guide the multilayer structure into the spatiotemporal regime<sup>1-4,49</sup>.

### Methods

#### Derivation of Eq. 4

The input-output relation of the band-unfolding operation can be written by

$$\begin{pmatrix} O_{k_1} \\ O_{k_2} \end{pmatrix} = \begin{pmatrix} P_{11} & P_{12} \\ P_{21} & P_{22} \end{pmatrix} \begin{pmatrix} I_o \\ I_e \end{pmatrix}, \quad (17)$$

where  $(I_o, I_e)^T$  is the initial wave state,  $O_{k_1}, O_{k_2}$  is the final wave state, and  $P_{ij} = \langle \tilde{\psi}_i(k) | \psi_j(k) \rangle$  with  $|\tilde{\psi}_i(k)\rangle$  ( $|\psi_j(k)\rangle$ ) being the  $i$ -th ( $j$ -th) eigenstate of after (before) the band-folding operation. However, we can not directly obtain  $P_{ij}$  since  $|\tilde{\psi}_i(k)\rangle$  and  $|\psi_j(k)\rangle$  are Bloch waves with different periods. Nevertheless, we can obtain the eigenstates of  $H_1$  and  $H_2$  with the same lattice constant  $2l$  and then determine  $P_{ij}$  accordingly. The eigenstates of  $H_2$  are  $(1, 0)^T$  and  $(0, 1)^T$  which are given in the main text. For  $H_1$ , we can regard that the even number sites and odd number sites are different and the lattice constant is  $2l$ , and then obtain the eigenstates  $(\omega_{\pm}, k)$  whose corresponding eigenvectors are  $(1/\sqrt{2}, \pm 1/\sqrt{2})^T$ . One can find that  $(\omega_+, k)$  corresponds to  $(\omega_1, k_1)$  and  $(\omega_-, k)$  corresponds to  $(\omega_2, k_2)$ , and therefore determines  $P_{ij}$ .

#### Details of the temporal degenerate-state interference

Here, we give the details of the numerical simulation procedure for the temporal degenerate-state interference as shown in Fig. 2b. We set a Gaussian-shaped-like initial state  $c_m(t=0) = \exp[-(m-81)^2/40] \cdot \exp(ik_0 ml)$  with  $k_0 = 0.25\pi/l$  for odd number  $m$ , where  $m = 1, 2, \dots, 201$ . Note that the Gaussian-shaped-like initial state in the  $m$  space corresponds to a Gaussian-shaped-like distribution  $\tilde{k}(k_0)$  centered at  $k_0$  in the momentum space. For  $t \in [0, 6 \text{ g}^{-1}]$  the Hamiltonian of the system is  $H_2$  with  $g = 0.002$  and  $\varphi = 0$ . At  $t = 6 \text{ g}^{-1}$ , we switch the coupling from the next nearest neighbor one to the nearest neighboring one so that the Hamiltonian becomes  $H_1$  with  $\varphi = 0$ . The original state now projects into two new states with different momenta  $\tilde{k}(k_1)$  and  $\tilde{k}(k_2)$ . To achieve a time reversal operation<sup>16</sup>, we switch  $\varphi$  from 0 to  $\pi$  at  $t = 30 \text{ g}^{-1}$ . Meanwhile, we give an additional phase  $\theta$  to the  $\tilde{k}(k_1)$  component. Such an additional phase shift can be obtained by firstly performing the Fast Fourier transformation (FFT) on  $c_m$  at the time  $t = 30 \text{ g}^{-1}$  to obtain  $c_k(n)$  where  $n = 1, 2, \dots, 201$ , then multiplying a phase factor  $e^{i\theta}$  for  $c_k(n)$  at  $0 < k < 3\pi/4l$ , and finally performing an inverse FFT to obtain the new  $c'_m(t = 30 \text{ g}^{-1})$ . We show the FFT  $c_k$  from  $c_m(t = 30 \text{ g}^{-1})$  and corresponding phase shift  $\theta(n)$  of different  $c_k$  in Fig. 8. Lastly, we change both the coupling range and coupling phase so that the Hamiltonian returns back to  $H_2$  in the main text with  $\varphi = 0$ . In addition, the phase shift operation can be approximately applied by directly multiplying the phase factor  $e^{i\theta}$  to  $c_m(t = 30 \text{ g}^{-1})$  for  $0 < m < 101$  since the states  $\tilde{k}(k_1)$  and  $\tilde{k}(k_2)$  are separated in the  $m$  space (Fig. 2b). Such an operation may help to apply phase shift on one of the modes in the momentum space.

Moreover, all the simulation results based on the TB method are performed by the rigorous numerical method. No analytical solution of the temporal interfaces is applied in the numerical simulation. The boundary condition of the Hamiltonian we use for band-folding

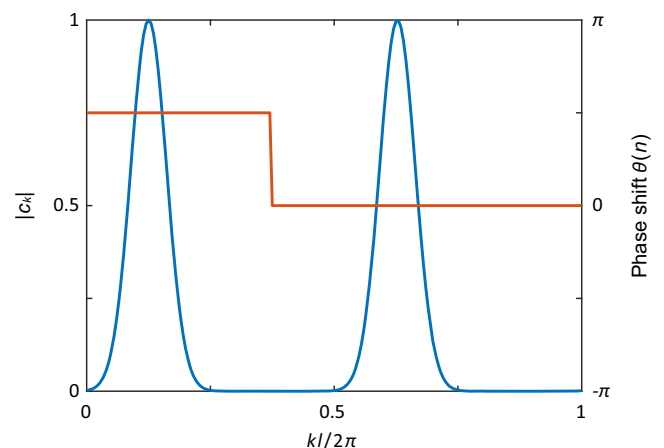


**Fig. 8 | Illustration of the phase shift operation in the momentum space.** Blue line:  $|c_k|$  at  $t = 30 \text{ g}^{-1}$ . Red line: additional phase  $\theta(n)$  for different  $k$  components.

operation is

$$H = \begin{cases} H_1 & t \leq t_0 \\ H_2 & t > t_0 \end{cases}, \quad (18)$$

where  $t_0$  is the corresponding time of the temporal interface. The boundary condition for band-unfolding operation is similar. The boundary condition of the coupling phase for the time reversal operation is

$$\varphi = \begin{cases} 0 & t \leq t_0 \\ \pi & t > t_0 \end{cases}. \quad (19)$$

Although we show the sharp change has been used in simulations for Figs. 2 and 3, the influence of the sharpness of these temporal interfaces on the interference in simulations are discussed in the supplementary material Section VIII.

## Data availability

The data generated in this study have been deposited in the figshare database under accession code [<https://doi.org/10.6084/m9.figshare.25479529>].

## Code availability

The codes used to process the data generated in this study are available in figshare under accession code [<https://doi.org/10.6084/m9.figshare.25479529>].

## References

- Galiffi, E. et al. Photonics of time-varying media. *Adv. Ed. Photonics* **4**, 014002 (2022).
- Yin, S., Galiffi, E. & Alù, A. Floquet metamaterials. *eLight* **2**, 1 (2022).
- Yuan, L. & Fan, S. Temporal modulation brings metamaterials into new era. *Light Sci. Appl.* **11**, 173 (2022).
- Engheta, N. Four-dimensional optics using time-varying metamaterials. *Science* **379**, 1190 (2023).
- Mendonça, J. & Shukla, P. Time refraction and time reflection: two basic concepts. *Phys. Scr.* **65**, 160 (2002).
- Plansinis, B., Donaldson, W. & Agrawal, G. What is the temporal analog of reflection and refraction of optical beams? *Phys. Rev. Lett.* **115**, 183901 (2015).
- Akbarzadeh, A., Chamanara, N. & Caloz, C. Inverse prism based on temporal discontinuity and spatial dispersion. *Opt. Lett.* **43**, 3297 (2018).
- Ramaccia, D., Toscano, A. & Bilotti, F. Light propagation through metamaterial temporal slabs: reflection, refraction, and special cases. *Opt. Lett.* **45**, 5836 (2020).
- Solís, D. M., Kastner, R. & Engheta, N. Time-varying materials in the presence of dispersion: plane-wave propagation in a lorentzian medium with temporal discontinuity. *Photon. Res.* **9**, 1842 (2021).
- Xu, J., Mai, W. & Werner, D. H. Complete polarization conversion using anisotropic temporal slabs. *Opt. Lett.* **46**, 1373 (2021).
- Ramaccia, D., Alù, A., Toscano, A. & Bilotti, F. Temporal multilayer structures for designing higher-order transfer functions using time-varying metamaterials. *Appl. Phys. Lett.* **118**, 101901 (2021).
- Pacheco-Peña, V. & Engheta, N. Temporal aiming. *Light Sci. Appl.* **9**, 129 (2020).
- Pacheco-Peña, V. & Engheta, N. Antireflection temporal coatings. *Optica* **7**, 323 (2020).
- Apffel, B. & Fort, E. Frequency conversion cascade by crossing multiple space and time interfaces. *Phys. Rev. Lett.* **128**, 064501 (2022).
- Yin, S., Wang, Y.-T. & Alù, A. Temporal optical activity and chiral time-interfaces. *Opt. Express* **30**, 47933 (2022).
- Yuan, L., Xiao, M. & Fan, S. Time reversal of a wave packet with temporal modulation of gauge potential. *Phys. Rev. B* **94**, 140303 (2016).
- Wang, S. et al. High-order dynamic localization and tunable temporal cloaking in ac-electric-field driven synthetic lattices. *Nat. Commun.* **13**, 7653 (2022).
- Long, O. Y., Wang, K., Dutt, A. & Fan, S. Time reflection and refraction in synthetic frequency dimension. *Phys. Rev. Res.* **5**, L012046 (2023).
- Wang, S. et al. Photonic floquet landau-zener tunneling and temporal beam splitters. *Sci. Adv.* **9**, eadh0415 (2023).
- Ye, H. et al. Reconfigurable refraction manipulation at synthetic temporal interfaces with scalar and vector gauge potentials. *Proc. Natl Acad. Sci. USA* **120**, e2300860120 (2023).
- Christodoulides, D. N., Lederer, F. & Silberberg, Y. Discretizing light behaviour in linear and nonlinear waveguide lattices. *Nature* **424**, 817 (2003).
- Aharonov, Y. & Bohm, D. Significance of electromagnetic potentials in the quantum theory. *Phys. Rev.* **115**, 485 (1959).
- Berry, M. V. Quantal phase factors accompanying adiabatic changes. *Proc. R. Soc. Lond. A. Math. Phys. Sci.* **392**, 45 (1984).
- Cohen, E. et al. Geometric phase from aharonov-bohm to pancharatnam-berry and beyond. *Nat. Rev. Phys.* **1**, 437 (2019).
- Osterloh, K., Baig, M., Santos, L., Zoller, P. & Lewenstein, M. Cold atoms in non-abelian gauge potentials: From the hofstadter" moth" to lattice gauge theory. *Phys. Rev. Lett.* **95**, 010403 (2005).
- Terças, H., Flayac, H., Solnyshkov, D. & Malpuech, G. Non-abelian gauge fields in photonic cavities and photonic superfluids. *Phys. Rev. Lett.* **112**, 066402 (2014).
- Chen, Y. et al. Non-abelian gauge field optics. *Nat. Commun.* **10**, 3125 (2019).
- Zhang, W., Wang, H., Sun, H. & Zhang, X. Non-abelian inverse anderson transitions. *Phys. Rev. Lett.* **130**, 206401 (2023).
- Yan, Q. et al. Non-abelian gauge field in optics. *Adv. Opt. Photon.* **15**, 907 (2023).
- Wu, T. T. & Yang, C. N. Concept of nonintegrable phase factors and global formulation of gauge fields. *Phys. Rev. D.* **12**, 3845 (1975).
- Horváthy, P. Non-abelian aharonov-bohm effect. *Phys. Rev. D.* **33**, 407 (1986).
- Yang, Y. et al. Synthesis and observation of non-abelian gauge fields in real space. *Science* **365**, 1021 (2019).
- Wu, J. et al. Non-abelian gauge fields in circuit systems. *Nat. Electron.* **5**, 635 (2022).
- Nayak, C., Simon, S. H., Stern, A., Freedman, M. & Sarma, S. D. Non-abelian anyons and topological quantum computation. *Rev. Mod. Phys.* **80**, 1083 (2008).
- Regensburger, A. et al. Parity-time synthetic photonic lattices. *Nature* **488**, 167 (2012).
- Peierls, R. Zur theorie des diamagnetismus von leitungselektronen. *Z. für Phys.* **80**, 763 (1933).
- Dalibard, J., Gerbier, F., Juzeliūnas, G. & Öhberg, P. Colloquium: artificial gauge potentials for neutral atoms. *Rev. Mod. Phys.* **83**, 1523 (2011).
- Goldman, N., Juzeliūnas, G., Öhberg, P. & Spielman, I. B. Light-induced gauge fields for ultracold atoms. *Rep. Prog. Phys.* **77**, 126401 (2014).
- Zohar, E., Cirac, J. I. & Reznik, B. Quantum simulations of lattice gauge theories using ultracold atoms in optical lattices. *Rep. Prog. Phys.* **79**, 014401 (2015).
- Ruseckas, J., Juzeliūnas, G., Öhberg, P. & Fleischhauer, M. Non-abelian gauge potentials for ultracold atoms with degenerate dark states. *Phys. Rev. Lett.* **95**, 010404 (2005).
- Polimeno, L. et al. Experimental investigation of a non-abelian gauge field in 2d perovskite photonic platform. *Optica* **8**, 1442 (2021).

42. Hasan, M. et al. Wave packet dynamics in synthetic non-abelian gauge fields. *Phys. Rev. Lett.* **129**, 130402 (2022).
43. Sun, Y.-K. et al. Non-abelian thouless pumping in photonic waveguides. *Nat. Phys.* **18**, 1080 (2022).
44. Mallesh, K. et al. A generalized pancharatnam geometric phase formula for three-level quantum systems. *J. Phys. A: Math. Gen.* **30**, 2417 (1997).
45. Goyal, S. K., Simon, B. N., Singh, R. & Simon, S. Geometry of the generalized bloch sphere for qutrits. *J. Phys. A: Math. Theor.* **49**, 165203 (2016).
46. Rechtsman, M. C. et al. Photonic floquet topological insulators. *Nature* **496**, 196 (2013).
47. Song, W. et al. Dispersionless coupling among optical waveguides by artificial gauge field. *Phys. Rev. Lett.* **129**, 053901 (2022).
48. Piao, X., Yu, S. & Park, N. Programmable photonic time circuits for highly scalable universal unitaries. *Phys. Rev. Lett.* **132**, 103801 (2024).
49. Mikheeva, E. et al. Space and time modulations of light with meta-surfaces: recent progress and future prospects. *ACS Photon.* **9**, 1458 (2022).
50. Sharabi, Y., Dikopoltsev, A., Lustig, E., Lumer, Y. & Segev, M. Spatiotemporal photonic crystals. *Optica* **9**, 585 (2022).
51. Yuan, L., Lin, Q., Xiao, M. & Fan, S. Synthetic dimension in photonics. *Optica* **5**, 1396 (2018).
52. Lustig, E. & Segev, M. Topological photonics in synthetic dimensions. *Adv. Opt. Photon.* **13**, 426 (2021).
53. Yang, M., Xu, J.-S., Li, C.-F. & Guo, G.-C. Simulating topological materials with photonic synthetic dimensions in cavities. *Quant. Front.* **1**, 10 (2022).
54. Ehrhardt, M., Weidemann, S., Maczewsky, L. J., Heinrich, M. & Szameit, A. A perspective on synthetic dimensions in photonics, *Laser Photon. Rev.* **17**, 2200518 (2023).
55. Hazzard, K. R. & Gadway, B. Synthetic dimensions. *Phys. Today* **76**, 62 (2023).
56. Wimmer, M., Price, H. M., Carusotto, I. & Peschel, U. Experimental measurement of the berry curvature from anomalous transport. *Nat. Phys.* **13**, 545 (2017).
57. Weidemann, S., Kremer, M., Longhi, S. & Szameit, A. Topological triple phase transition in non-hermitian floquet quasicrystals. *Nature* **601**, 354 (2022).
58. Leefmans, C. et al. Topological dissipation in a time-multiplexed photonic resonator network. *Nat. Phys.* **18**, 442 (2022).
59. Dutt, A. et al. Experimental band structure spectroscopy along a synthetic dimension. *Nat. Commun.* **10**, 3122 (2019).
60. Yuan, L., Dutt, A. & Fan, S. Synthetic frequency dimensions in dynamically modulated ring resonators. *APL Photon.* **6**, 071102 (2021).
61. Li, G. et al. Observation of flat-band and band transition in the synthetic space. *Adv. Photon.* **4**, 036002 (2022).
62. Englebort, N. et al. Bloch oscillations of coherently driven dissipative solitons in a synthetic dimension. *Nat. Phys.* **19**, 1014 (2023).
63. Senanian, A., Wright, L. G., Wade, P. F., Doyle, H. K. & McMahon, P. L. Programmable large-scale simulation of bosonic transport in optical synthetic frequency lattices. *Nat. Phys.* **19**, 1333 (2023).
64. Cheng, D., Lustig, E., Wang, K. & Fan, S. Multi-dimensional band structure spectroscopy in the synthetic frequency dimension. *Light Sci. Appl.* **12**, 158 (2023).
65. Li, G. et al. Direct extraction of topological zak phase with the synthetic dimension. *Light Sci. Appl.* **12**, 81 (2023).
66. Dong, P. Silicon photonic integrated circuits for wavelength-division multiplexing applications. *IEEE J. Sel. Top. Quant. Electron.* **22**, 370 (2016).
67. Pellerin, F., Houvenaghel, R., Coish, W., Carusotto, I. & St-Jean, P. Wave-function tomography of topological dimer chains with long-range couplings. *Phys. Rev. Lett.* **132**, 183802 (2024).
68. Cheng, D. et al. Non-Abelian lattice gauge fields in the photonic synthetic frequency dimension. *arXiv preprint arXiv:2406.00321* (2024).
69. Moussa, H. et al. Observation of temporal reflection and broadband frequency translation at photonic time interfaces. *Nat. Phys.* **19**, 863 (2023).
70. Dong, Z. et al. Quantum time reflection and refraction of ultracold atoms. *Nat. Photon.* **18**, 68 (2024).

## Acknowledgements

The research was supported by National Natural Science Foundation of China (12122407, 11974245, and 12192252), National Key Research and Development Program of China (No. 2023YFA1407200 and No. 2021YFA1400900). L.Y. thanks the sponsorship from the Yangyang Development Fund.

## Author contributions

Z.D. initiated the idea and performed the simulation. Z.D., X.W., Y.Y., P.Y., and L.Y. discussed the results. Z.D. and L.Y. wrote the draft. Z.D., X.W., Y.Y., P.Y., L.Y., and X.C. revised the manuscript. L.Y. supervised the project.

## Competing interests

The authors declare no competing interests.

## Additional information

**Supplementary information** The online version contains supplementary material available at <https://doi.org/10.1038/s41467-024-51712-z>.

**Correspondence** and requests for materials should be addressed to Luqi Yuan.

**Peer review information** *Nature Communications* thanks Yi Yang, Emanuele Galiffi, and the other, anonymous, reviewer(s) for their contribution to the peer review of this work. A peer review file is available.

**Reprints and permissions information** is available at <http://www.nature.com/reprints>

**Publisher's note** Springer Nature remains neutral with regard to jurisdictional claims in published maps and institutional affiliations.

**Open Access** This article is licensed under a Creative Commons Attribution-NonCommercial-NoDerivatives 4.0 International License, which permits any non-commercial use, sharing, distribution and reproduction in any medium or format, as long as you give appropriate credit to the original author(s) and the source, provide a link to the Creative Commons licence, and indicate if you modified the licensed material. You do not have permission under this licence to share adapted material derived from this article or parts of it. The images or other third party material in this article are included in the article's Creative Commons licence, unless indicated otherwise in a credit line to the material. If material is not included in the article's Creative Commons licence and your intended use is not permitted by statutory regulation or exceeds the permitted use, you will need to obtain permission directly from the copyright holder. To view a copy of this licence, visit <http://creativecommons.org/licenses/by-nc-nd/4.0/>.

© The Author(s) 2024